

Functionalities of Au_2O , Au_2O_3 , $\text{Au}_2\text{O}_{3-x}$, and nanosheets, including spontaneous polarization, using DFT and hybrid functional

Yukio Watanabe*

Kyushu University, Shiobara, Minami-ku, Fukuoka, Japan 815-8540
University of Hyogo, Shosya, Himeji, Hyogo, Japan 671-2201

We used density functional theories (DFT) to investigate the properties of Au_2O and $\text{Au}_2\text{O}_{3-x}$ ($x = 0\text{--}0.08$) to reveal their remarkable functionalities. Hybrid functional theories accurately estimate the band gap (E_g) of oxides, and the present hybrid functional calculations determined E_g values of 0.96 eV for Au_2O and 2.86 eV for Au_2O_3 , which is $>300\%$ of the commonly accepted E_g of Au_2O_3 (0.85 eV). Moreover, we discovered spontaneous polarization (P_s) in Au_2O_3 , which is unusually large and advantageous for catalysis. The P_s was retained even in 2-nm-thick Au_2O_3 nanosheets, similar to hyperferroelectric, generating a potential of 0.6 eV despite screening caused by surface reconstruction, which is a novel screening mechanism. Below a thickness of 0.8 nm, the P_s vanished, and inversion symmetry emerged at 0.4 nm, suggesting a new approach to finding a paraelectric phase. Au_2O was supersoft under shear distortion.

This is an accepted manuscript. Physics Letters A **573**, 131367 (2026)
Journal page: <https://doi.org/10.1016/j.physleta.2026.131367>

Keywords: Au_2O_3 Au_2O band gap ferroelectric depolarization size effect screening mechanisms

I. Introduction

Among noble metals, Au is widely recognized for its chemical inertness and exceptional resistance to oxidation. This property makes Au suitable for diverse applications, such as in semiconductors [1], biomedical devices [2], and electrochemical systems [3]. However, in certain electrochemical reactions, the surfaces of Au anodes undergo oxidation [4]. Additionally, during manufacturing processes, Au-deposited materials are often annealed in oxidizing environments. Similar oxidation of Au surfaces has also been observed in plasma [5], ozone [6], and high-temperature O₂ atmospheres [7]. Upon oxidation, Au surfaces exhibit notable catalytic activity, and the essential role of oxygen in this behavior has been well documented [8].

To elucidate the properties of oxidized Au surfaces, oxygen-chemisorbed Au surfaces [6–9] and Au oxides have been extensively investigated. However, only limited studies have focused on bulk Au oxides [6,10–20]. In particular, these studies have examined the Au¹⁺, Au²⁺, Au³⁺, and Au⁴⁺ oxidation states of bulk Au–O compounds. Of these, only Au₂O₃ and Au₂O have been synthesized experimentally in bulk form [10–13]. Specifically, Au₂O₃ was synthesized under hydrothermal conditions by Schwarzmüller et al. [10] and Weiher et al. [13]. Schwarzmüller et al. [11] also synthesized single crystals of Au₂O₃, while Jones et al. [12] subsequently determined their crystal structures. Higo et al. [14] showed that gold surfaces became Au₂O₃ after the exposure to an oxygen glow discharge. Irissou et al. [15] reported that their vacuum-deposited Au oxide films consisted of Au₂O₃. Further, Pireaux et al. [6] observed that heating Au₂O₃ to approximately 450 K initiated decomposition, yielding Au₂O as a breakdown product.

Beyond experimental studies, theoretical investigations have elucidated the structural and electronic properties of Au₂O₃ and Au₂O and predicted those of their pure stoichiometric phases. For instance, Joshi et al. [16] and Tang et al. [17] used density functional theory (DFT) and the force field method to demonstrate that Au₂O₃ is stable under the pressure of 0–50 GPa, whereas Au₂O can metastably exist under the pressure of 25–50 GPa. Filippetti and Fiorentini [18] observed that, according to DFT calculations, the cubic phase of Au₂O was more stable than its face-centered cubic counterpart. Zhang et al. [19] and Tang et al. [17] predicted the existence and structure of hypothetical AuO₄ using DFT, while Hermann et al. [20] investigated the structural, electronic, and dynamic properties of hypothetical AuO using hybrid functional theory [21, 22]. Further, a

DFT study conducted by Ren et al. [23] clarified the mechanism underlying the selective oxidation of vinyl chloride on Au_2O (100) surfaces.

Additionally, Pei et al. [24] reported the optical properties, including the dielectric functions, of Cu_2O , Ag_2O , and Au_2O using DFT. Using the generalized gradient approximation (GGA), Pei et al. [24] and Shi et al. [25] estimated the band gaps of Au_2O and Au_2O_3 , which were small and have been used as reference values. However, DFT calculations, including those performed using GGA, are known to inadequately account for electron correlation effects and fail to eliminate electron self-interactions, leading to inaccurate electronic and magnetic properties and erroneous band gap predictions. These deficiencies are effectively resolved by hybrid functionals, as demonstrated by numerous studies [21, 22, 26–30].

Meanwhile, spontaneous polarization (P_s) has been shown to facilitate efficient photocatalytic water splitting by spatially separating photogenerated electrons (e^-) and holes (h^+) [31, 32], while magnetism and spin ordering are thought to enhance catalytic activity [33].

Although bulk forms of Au oxides have been experimentally observed only in Au_2O_3 and Au_2O [10–13], with Au_2O_3 considered the most important, the theoretical investigations of their properties have been limited to a few. Hence, we investigate their structural, dielectric, mechanical, electronic, and magnetic properties using DFT and hybrid functionals. These calculations reveal a high degree of functionality in these oxides, including pronounced P_s and hyperferroelectric-like behavior in Au_2O_3 . Furthermore, the hybrid functional calculations demonstrate that Au_2O_3 is an insulator with a band gap (E_g) sufficiently large to support dielectric and optical applications.

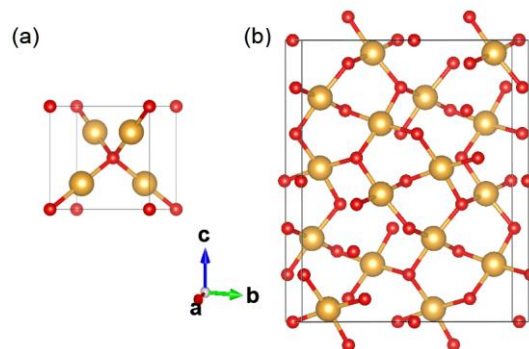


Fig. 1. Atomic positions in (a) Au_2O and (b) Au_2O_3 unit cells. Au and oxygen atoms are represented by large yellow and small red circles, respectively. This color scheme is maintained in all subsequent figures.

II. Methods

Au_2O has a cuprite structure (cubic, $\text{Pn}-3\text{m}$ symmetry), and its unit cell contains four Au and two O atoms [18, 23, 24]. Au_2O_3 is orthorhombic ($\text{Fdd}2$ symmetry), and its unit cell consists of 16 Au and 24 O atoms [12] (Fig. 1). DFT(GGA) and hybrid functional calculations used PAW potentials [34] implemented in VASP [35–37]. The plane wave energy cutoff was 650 eV, and a Gaussian function with a temperature broadening (σ) of 0.05 eV. We used Perdew-Burke-Ernzerhof functional optimized for solids (PBEsol) [38] as GGA and the Heyd - Scuseria - Ernzerhof functional for solids (HSEsol) [21] as the hybrid functional. The screening parameter (μ) in HSEsol is the default value (0.2 \AA^{-1}), and the k -grid reduction option of the Hartree-Fock kernel (Nkred) for reducing computational cost was not used in calculations of bulk Au_2O_3 and Au_2O . The PAW potentials were those recommended by the VASP manual for solid metal oxides: Au PAW potential for Au and O_s PAW potential for O in oxides with a cutoff energy of 282.85 eV.

The Monkhorst-Pack k -mesh for Brillouin-zone integration [39] in the geometry relaxation was $8 \times 8 \times 8$ for Au_2O and $7 \times 3 \times 3$ for Au_2O_3 . All the ion positions were relaxed without restriction, and all the calculated forces were lower than 3 meV/ \AA after relaxation. P_S was calculated using a Berry phase method [40] as implemented in VASP. The equilibrium lattice parameters calculated using PBEsol are often different from those using HSEsol [27, 29, 41]. However, in the case of Au oxides, such a difference was negligible; the equilibrium lattice constants of Au_2O calculated using PBEsol and HSEsol were 4.69 \AA and 4.69 \AA , respectively, and the equilibrium lattice constants of Au calculated using PBEsol and HSEsol were 4.08 \AA and 4.09 \AA , respectively. Hence, we used the lattice parameters calculated using PBEsol for the HSEsol calculations of electronic properties.

In addition to bulk Au_2O and Au_2O_3 , a -surfaces (surfaces perpendicular to the a -axis) of Au_2O_3 in a vacuum were calculated using slab supercells. The vacuum width was 30 \AA , which was sufficiently wider than the frequently used width (15 \AA). For these supercells, the Monkhorst-Pack k -mesh [39] in the geometry relaxation was $1 \times 3 \times 3$. A graphics-processing-unit acceleration [42, 43] was employed for calculations of Au_2O_3 . Ion positions are displayed using VESTA [44].

Table 1. Lattice constants obtained from this study, experimental report [12], and previous DFT studies. The deviations of the theoretical values from the experimental values are shown in δ .

Au ₂ O	This work	DFT ^a	DFT ^b	DFT ^c	DFT ^d
<i>a</i> (Å)	4.69	4.78	4.82	4.81	4.80

Au ₂ O ₃	Experiment (Å)	This work (Å)	δ (%)	DFT ^d (Å)	δ (%)
<i>a</i> (Å)	3.838	3.906	1.77	4.038	5.21
<i>b</i> (Å)	10.520	10.490	0.29	10.685	1.57
<i>c</i> (Å)	12.827	12.840	0.10	13.057	1.79

^a Ren et al. [23]. ^b Pei et al. [24]. ^c Filippetti and Fiorentini [18]. ^d Shi et al. [25].

III. Results and Discussion

1. Structural, elastic, and phonon properties

The only experimental data available for the physical properties of Au₂O₃ and Au₂O pertain to crystal structures, bond lengths, and compositions determined by X-ray photoemission [10–15]. Therefore, the only experimental comparisons made in this study involve lattice constants, which are directly related to bond lengths. The computed equilibrium lattice constants are presented in Table 1. This table indicates that the lattice constants of Au₂O and Au₂O₃ calculated using DFT (PBEsol) in this study are smaller than those reported in previous ones [18, 23–25].

Most GGAs are known to overestimate the lattice constants of solids [38], while calculations using PBEsol yield more accurate values for both lattice constants and ferroelectric properties [27, 29, 30, 38, 41]. The calculated lattice constants of Au₂O₃ in this study using PBEsol exhibited better agreement with experimental values than those reported previously [25]. The discrepancies between the present and earlier results arise from variations in the GGA functional used. Meanwhile, calculations performed using the conventional GGA (PBE) in this study yielded a lattice constant of 4.78 Å for Au₂O, consistent with prior reports [18, 23–25].

Table 2 presents the elastic compliance coefficients (C_{ij}) calculated using the GGA (PBEsol). These C_{ij} coefficients are compared with those of well-known oxides, SrTiO₃ and BaTiO₃, since no literature on the elastic properties of Au oxides was found except for the bulk modulus of Au₂O [24] and C_{ij} of Au₂O₃ listed in Materials Project [45]. The C_{ij} coefficients of Au₂O for compression/expansion (C₁₁, C₁₂) are markedly smaller than those for SrTiO₃ and BaTiO₃. The

bulk modulus of Au_2O , calculated [46] as 119 GPa using C_{11} and C_{12} from [Table 2](#), is comparable to the previously reported value of 97 GPa [24]. Notably, the C_{ij} coefficient for shear distortion (C_{44}) is almost zero, indicating an exceptionally soft response to shear stress. The C_{ij} coefficients of Au_2O_3 for compression and expansion (C_{ij} : $i, j \leq 3$) are slightly smaller than those of SrTiO_3 and BaTiO_3 , while the shear distortion coefficients (C_{ii} : $i \geq 4$) are substantially lower. These C_{ii} values are slightly larger than those in Materials Project [45].

Table 2. Elastic compliance coefficients (GPa) obtained in the present study compared with those of cubic SrTiO_3 and tetragonal BaTiO_3 [31]. For comparison with Materials Project, the exchange of the indices 1–6 is needed.

	C_{11}	C_{12}	C_{13}	C_{22}	C_{23}	C_{33}	C_{44}	C_{55}	C_{66}
Au_2O	123	117					3		
Au_2O_3	85	83	74	203	79	225	35	61	45
SrTiO_3	349	103					114		
BaTiO_3	299	111	85			136	125		107

The calculated zone-center phonon modes of Au_2O occur at energies of 76, 61, 26, 14, 10, and 6 meV ($1 \text{ meV} = 8.066 \text{ cm}^{-1} = 0.2418 \text{ Tz}$) and include three soft modes, whereas the previously reported energies were 70, 56, 25, 13, 10, and 6 meV [25]. Meanwhile, for Au_2O_3 , the highest-energy zone-center phonon mode, at 72 meV [25], and phonon dispersions [45] are previously reported. We find that the zone-center phonon modes are grouped into “nearly continuous” bands, namely 61–75 meV, 39–44 meV, 36 meV, and 11–31 meV, and also include three soft modes. The first band comprises 48 modes: one at 75 meV, four at 74 meV, four at 73 meV, two at 72 meV, twelve at 71 meV, one at 70 meV, one at 68 meV, three at 67 meV, four at 66 meV, six at 65 meV, two at 64 meV, four at 63 meV, three at 62 meV, and one at 61 meV. The second band contains 15 modes: three at 44 meV, five at 43 meV, two at 42 meV, one at 40 meV, and four at 39 meV. The third band contains one mode at 36 meV. The fourth band contains 53 modes: two at 31 meV, three at 29 meV, six at 27 meV, six at 23–25 meV, sixteen at 20–22 meV, six at 17–19 meV, four at 16 meV, six at 12–13 meV, and four at 11 meV. These values are consistent with phonon dispersions in Au_2O_3 [45]. For example, in SrTiO_3 and BaTiO_3 , the phonon energies calculated using PBEsol tend to agree better with the experimental values than those calculated using PBE [27].

Table 3. E_g values obtained in this work (HSEsol) and previous studies a–e. a, b, d, e: GGA. c: screened-exchange LDA. In ref. [25], $E_F - E_V$, which should be zero, is approximately 0.4 eV for Au_2O_3 .

	This work	DFT	DFT
Au_2O	0.96	0 ^a	0 ^b , 0.83 ^c
Au_2O_3	2.86		0.85 ^d , 0.85 ^e

^a Pei et al. [24]. ^{b–d} Shi et al. [25]. ^e Materials Project [45].

2. Electronic structures

The band structures and density of states (DOS) were calculated using the hybrid functional HSEsol and the GGA-based DFT (PBEsol). Xiao et al. [26] reported a strong agreement between the E_g values computed using hybrid functionals and through experiments for various semiconductors. To illustrate the accuracy of hybrid functionals for oxides, we compare the indirect band gaps obtained from experiments (exp.), hybrid functionals (HSE [22] or HSEsol [21]), and GGA-based DFT. Notably, the E_g values calculated using HSE/HSEsol agree with experimental values, within approximately 0.2 eV. For cubic SrTiO_3 , the E_g values are 3.25 eV (exp.), 3.07 eV (HSE), and 1.80 eV (GGA); meanwhile, for tetragonal BaTiO_3 , the E_g values are 3.4 eV (exp.), 3.31 eV (HSEsol), and 1.76 eV (GGA) [27, 29].

The band diagrams and DOS of pure stoichiometric Au_2O and Au_2O_3 are presented in Figs. 2 and 3. Throughout, all energies are measured relative to the Fermi level (E_F). Meanwhile, the E_g values obtained in this and previous studies are compared in Table 3. In the *ab initio* results for 0 K, E_F corresponds to the highest occupied states; for insulators, E_F lies at the top of the valence band (E_V) [17, 18, 24, 45], which differs from the definition of E_F in semiconductor physics [1].

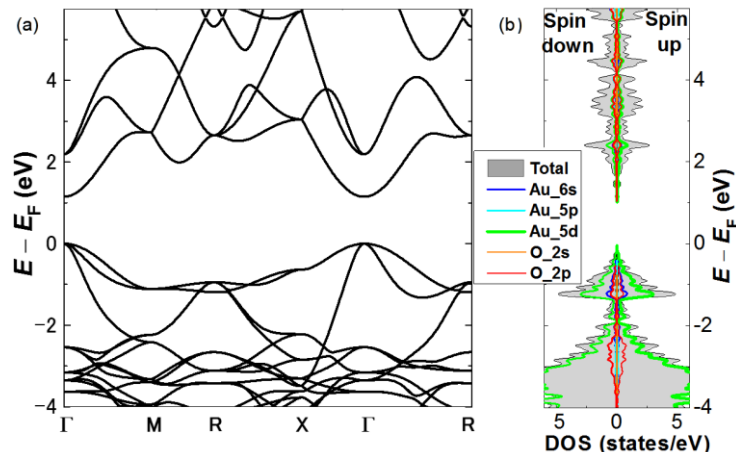


Fig. 2. Band structure (a) and projected DOS (b) of Au_2O calculated using the hybrid functional (HSEsol).

The relative positions of the bands of Au_2O were similar to those calculated using GGA [24] and the screened-exchange LDA [25]. For example, the band gap of Au_2O occurs at the Γ point and is a direct gap (Fig. 2(a)), agreeing with the previous reports [24, 25]. However, the calculated E_g value is 0.96 eV, which is >20% greater than the values in these studies [24, 25] (Table 1). When calculated using the GGA (PBEsol), E_g was zero, consistent with the calculations using GGA [24, 25]. In both Au_2O and Au_2O_3 , the DOS of both Au_2O and Au_2O_3 consists primarily of $\text{Au}_{5\text{d}}$ and $\text{O}_{2\text{p}}$ orbitals in the energy range from -4 eV to 5 eV, and magnetic ordering is absent, as the projected DOSs and band diagrams are identical for their spin-up and spin-down states (Figs. 2(b) and 3(b)).

In Fig. 3(b), the DOSs of Au_2O_3 are divided by four because the number of Au atoms in Au_2O_3 is four times that in Au_2O . The band gap is indirect, consistent with previous studies [25, 45]. However, E_g is 2.86 eV (Figs. 3(a) and 3(b)), which suggests that a pure, stoichiometric Au_2O_3 crystal is transparent and nearly colorless. Contrastingly, Shi et al. [25] described Au_2O_3 as a semiconductor with $E_g = 0.85$ eV (Table 3), while the DOS in the same study [25] indicates $E_g \approx 0.5$ eV or less. When calculated using the GGA (PBEsol), the E_g value was 0.87 eV, consistent with Materials Project [45].

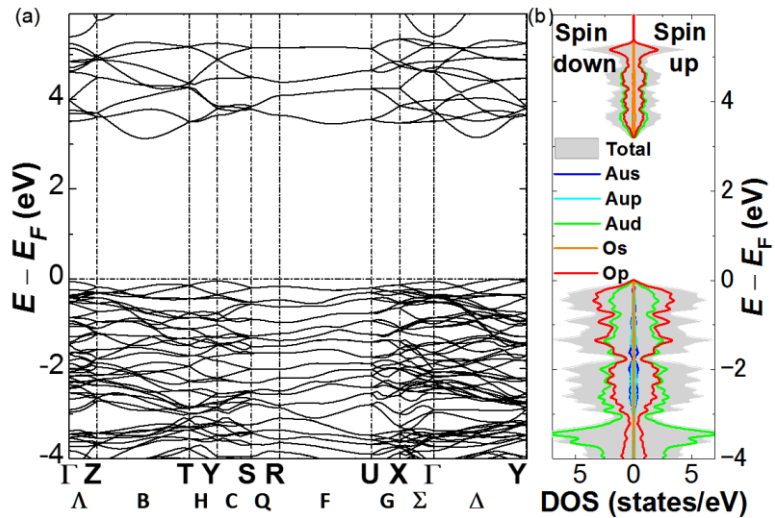


Fig. 3. Band structure (a) and projected DOS (b) of Au_2O_3 calculated using the hybrid functional (HSEsol). The original DOS is divided by four to obtain the displayed DOS to adjust the number of Au atoms in the unit cell (4 Au atoms in Au_2O and 16 Au atoms in Au_2O_3).

In the detailed analysis of [Fig. 3\(a\)](#), many bands are closely packed due to low structural symmetry, as previously reported [\[25,45\]](#). Consequently, several points in the Brillouin zone [\[47\]](#) exist near E_V (i.e., E_F) and the bottom of the conduction bands (E_C). Specifically, E_V is on the Γ –Y path, with the energies at Γ and Y close to E_V , while E_C lies on the T–Z path, with the energies on the Γ –Y path close to E_C . Although not shown in [Fig. 3\(a\)](#), the energies on the Γ –R, Γ –Z, and X–Y paths were also close to E_V , and the energies on the Γ –R and Γ –Z were also close to E_C , which was also found in the calculations using PBEsol.

[Figure 3\(a\)](#) can be favorably compared with the bands in Materials Project [\[45\]](#), using the high symmetry points present in both plots. For this comparison, we denote E_Γ and E_U as the highest energy at Γ below E_V and the lowest energy at U above E_C , respectively. $E_F - E_\Gamma$ is 70 meV in [Fig. 3\(a\)](#) and 130 meV in ref. [\[45\]](#), which can be considered as consistent with DOS. In [Fig. 3\(a\)](#), E_C lies on the T–Z path and is 0.42 eV lower than E_U , whereas in ref. [\[45\]](#), the T–Z path is absent, and E_C is only 0.14 eV lower than E_U . Hence, E_C as compared with E_U in [Fig. 3\(a\)](#) is much lower than E_C as compared with E_U in ref. [\[45\]](#), which presumably suggests that the band paths in conduction bands in [Fig. 3\(a\)](#) are approximately sufficient for estimating E_C .

A comparison between these results and those in ref. [\[25\]](#) is unfeasible because the band plots in [Fig. 3\(a\)](#) of ref. [\[25\]](#) are incomplete; specifically, the bands beneath E_F , which DOS in that figure indicates should be present, are missing. In that figure, the standard convention for E_F in insulators ($E_F = E_V$) appears to be applied, as $E_F = E_V$ in [Fig. 4](#) of the same study [\[25\]](#). Hence, the bands corresponding to the correct E_V are absent in [Fig. 3\(a\)](#) of ref. [\[25\]](#), which explains the discrepancy between the reported $E_g = 0.85$ eV [\[25\]](#), presumably obtained using $E_C - E_V$ and an incorrect E_V , and $E_g \approx 0.5$ eV calculated using $E_C - E_F$ or DOS in [Fig. 3\(a\)](#) of ref. [\[25\]](#).

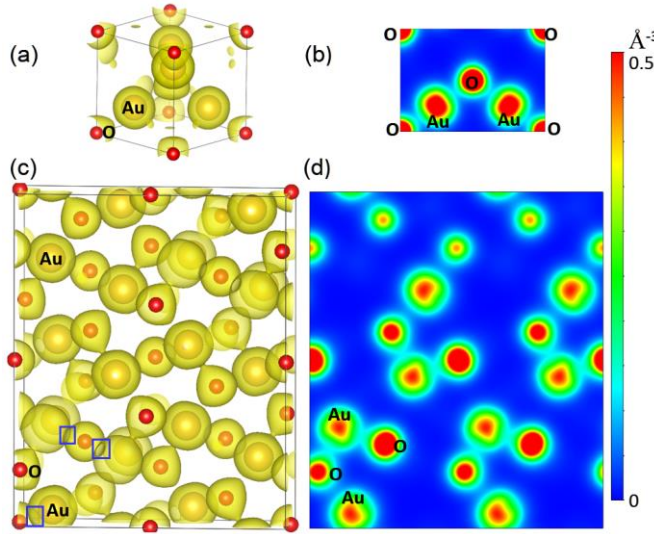


Fig. 4 Iso- e^- -density surfaces (0.12 \AA^{-3}) in Au_2O (a) and Au_2O_3 (c) and their cross-sections at the (110) plane ((b), (d)). The ovals at the boundaries of the O and Au orbits in (c) indicate that these orbits are in contact there, with examples marked by blue squares.

The greater stability of Au_2O_3 compared to Au_2O [6, 16, 17] indicates stronger bonding, i.e., increased hybridization between Au and O in Au_2O_3 . This is confirmed by the higher DOS and the stronger correlation between the Au_{5d} and O_{2p} orbitals just beneath E_F in Au_2O_3 compared to Au_2O , as shown in the DOS plots in Figs. 2(b) and 3(b). Consistently, many Au and O iso- e^- -density surfaces are in contact in Au_2O_3 in Fig. 4, whereas those in Au_2O are not, supporting the stronger bonding between Au and O atoms in Au_2O_3 . Furthermore, the atomic bonding (Fig. 1) shows that each Au atom is coordinated three-dimensionally with four O atoms in Au_2O_3 but one-dimensionally with only two O atoms in Au_2O . In particular, Au_2O consists solely of a *V*-shaped and an inverted-*V*-shaped Au-O bonds, their vertices contacted at an O atom (Figs. 1(a) and 4(a)). This bonding configuration is speculated to be rotationally deformable. Contrastingly, the bonding in SrTiO_3 and BaTiO_3 is three-dimensional, and the Ti_{3d} orbitals are highly directional. These features may explain the aforementioned supersoftness of Au_2O under shear strain.

The synthesis of Au_2O suitable for electrical or optical characterization has not yet been reported. Similarly, the synthesis of extremely stoichiometric Au_2O_3 remains challenging [13]; e.g., vacuum-deposited Au_2O_3 films were $\text{Au}_2\text{O}_{3-x}$ ($x = 0.17$) [15], whereas the theoretical studies of $\text{Au}_2\text{O}_{3-x}$ ($x > 0$) have not been reported. In light of these limitations, we present the DOS of $\text{Au}_2\text{O}_{3-x}$ ($x = 4\%, 8\%$), with the positions of the oxygen vacancies (V_O) indicated in Fig. 5.

The presence of V_o did not induce metallicity in Au_2O_3 (Fig. 5). However, a single V_o among 24 oxygen atoms ($x = 4\%$) lowers E_C to 1.5 eV, while two V_o species ($x = 8\%$) lower E_C to 1.3 eV. These results suggest that Au_2O_3 containing V_o species is expected to be a semiconductor and appear nearly black. The configuration with V_o species at positions 1 and 2 corresponds to a dispersive V_o distribution, whereas that with V_o species at positions 1 and 3 corresponds to an aggregated distribution. Notably, the free energy gain, i.e., the stability of the aggregated configuration is 0.2 eV per unit cell higher than that of the dispersive configuration.

V_o 's in Au_2O_3 create trap-like narrow bands near the original E_V and E_C , while both the valence and conduction bands near E_F and these narrow bands exhibit a mixture of O_{2p} and Au_{5d} character with nearly equal contributions. The V_o -related new band near E_V is ineffective as acceptors because it lies below E_F , and the V_o -related new bands near E_C are also ineffective as donors because they are located well above E_F . This behavior contrasts notably with that observed in Ti-oxides such as $SrTiO_3$, where the valence and conduction bands near E_F are predominantly of O_{2p} and Ti_{3d} character, respectively. In these oxides, the V_o -created donor states are of Ti_{3d} character and lie slightly below E_C , and the trapped e^- in these shallow states can be easily activated to become free e^- , which explains experimental properties well.

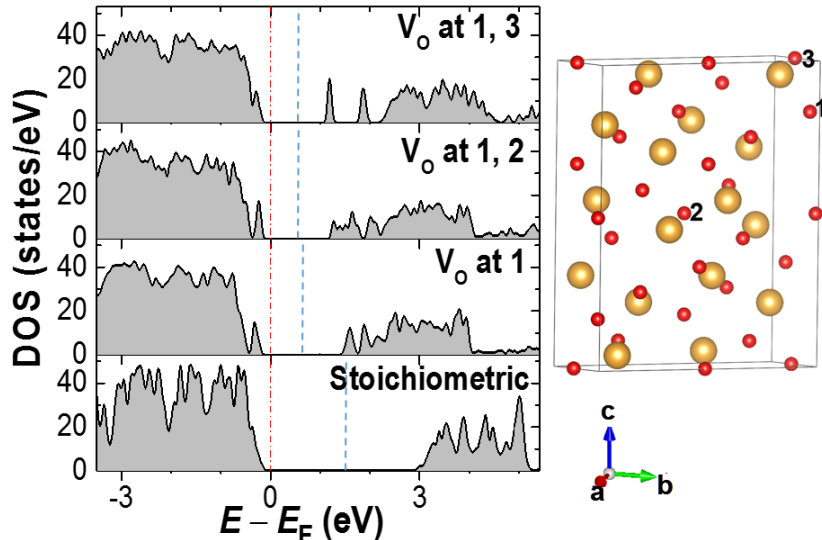


Fig. 5. DOS of Au_2O_3 with 4% and 8% oxygen vacancies (V_o) calculated with hybrid functional and the illustration of the position of V_o . The vertical red and blue lines show E_F in *ab initio* calculations for insulators and semiconductor physics, respectively [1].

3. P_S and dielectric properties

The electronic dielectric constant (ε), or the optical dielectric constant at zero energy, of Au_2O is 10.6 (Table 4), which is slightly higher than the previously reported value of $\varepsilon = 8.5$ [24]. The ε values of Au_2O_3 are comparable to those reported in Materials Project [45]. These ε values are considerably higher than those of the archetypal ferroelectric tetragonal BaTiO_3 and the archetypal paraelectric cubic SrTiO_3 ([48]), both of which are recognized as high-permittivity materials (Table 4).

Furthermore, the total dielectric constants under ion-clamped conditions are comparable to those of BaTiO_3 and SrTiO_3 : 11 for Au_2O ; 7, 12, and 11 for Au_2O_3 ; 7 and 28 for BaTiO_3 ; and 12 for SrTiO_3 .

Table 4. P_S ($\mu\text{C}/\text{cm}^2$) and ε along the a -, b -, and c -axes obtained in the present study, compared with values from previous studies. All data were calculated using GGA(PBEsol) except for 5.7 ^{c*}, which was calculated with DFT with Hubbard on-site potential [30] and agreed well with the experimental data at optical energy.

	P_{Sa}	P_{Sb}	P_{Sc}	ε_a	ε_b	ε_c	ε_a	ε_c
Au_2O	0	0	0	10.6			8.5 ^a	
Au_2O_3	213.8	0	0	6.6	11.0	9.9		
BaTiO_3	0	0	32.8 ^b				6.5 ^c	5.8 ^c
SrTiO_3							6.3 ^c , 5.7 ^{c*}	

^a Ref. [24]. ^b Ref. [30]. ^c Ref. [48].

We observed that the piezoelectric constants are zero for Au_2O but nonzero for Au_2O_3 , consistent with the absence of inversion symmetry in the latter. Likewise, P_S is zero for Au_2O but nonzero for Au_2O_3 (Table 4). As demonstrated in the comparison with BaTiO_3 in Table 4, the P_S of Au_2O_3 is substantial.

For reference, the experimental P_S of BaTiO_3 at 270 K is $26.9 \mu\text{C}/\text{cm}^2$, while the quasi-experimental P_S of BaTiO_3 at 0 K is $32 \mu\text{C}/\text{cm}^2$ [29], which serves as the appropriate benchmark for comparison with *ab initio* calculations [29]. Further, the P_S of BaTiO_3 reported in Table 4 agrees well with this reference P_S . In this context, recent outcomes [31, 32] report that potential produced by P_S can enhance photocatalysis when defect-free surfaces form without adsorbates. Furthermore, we speculate that Au_2O_3 -like atomic configurations may locally exist on oxygen-adsorbed Au surfaces and thereby contribute to catalytic activity.

These applications utilize free polar surfaces, to which P_S is perpendicular. In this case, P_S is shown to disappear or be substantially reduced by the depolarization field (E_d) arising from P_S [49–51]. This situation corresponds to a prototypical case of a ferroelectric wherein a freestanding ferroelectric is plate-like, placed in an infinite vacuum, free of adsorbates and defects, and of the single-domain with P_S perpendicular to the plate surface. In this case, $E_d = -P_S/\varepsilon_0$ (ε_0 : vacuum permittivity) and produces a macroscopic equilibrium potential difference $\Delta\phi^{eq}_{macro}$, when the ferroelectric is perfectly insulating. No additional permittivity should be inserted in $E_d = -P_S/\varepsilon_0$, when P_S stands for an all-inclusive or self-consistent spontaneous polarization [49].

In the Ginzburg–Landau (GL) framework for this case, the effect of E_d is expressed by an effective increase in the ambient temperature (T) [49]. The GL free energy is

$$F = (T - T_0)P^2/2C\varepsilon_0 + \beta P^4/4 + \gamma P^6/4 - PE_d/2,$$

where T_0 , C , β , and γ are Curie–Weiss temperature, Curie constant, and GL coefficients, respectively. Curie temperature T_C is $T_0 + \Delta T$, where $\Delta T = 3\beta^2/16\gamma C\varepsilon_0$. For 2nd order transition, $\gamma = 0$, $\beta > 0$, and $T_C = T_0$. The effect of E_d is the change of T_0 to $T_0 - C$ in F , or to $T_0 - C/\varepsilon_{NG}$ when the inaccuracy of the GL theory is corrected by a factor of $\varepsilon_{NG} > 1$ [49]. For almost all displacive-type ferroelectrics such as BaTiO₃ and PbTiO₃, $T_0 \ll C$, C/ε_{NG} , which means $P_S = 0$ and the emergence of an inversion symmetric phase in this situation.

Consequently, the previous studies [49–51] have demonstrated that, in the aforementioned situation, an insulating ferroelectric without external screening charges either transforms into a paraelectric phase (i.e., $P_S = 0$) or remains ferroelectric (i.e., $P_S \neq 0$), with the latter accompanied by the formation of e^- and h^+ layers. Hence, studies [50,51] have shown that the maximum $\Delta\phi^{eq}_{macro}$ ($\Delta\phi^{eq}_{macro}^{max}$) generated by P_S , corresponding to $\Delta\phi^{eq}_{macro}$ between the P_S^+ and P_S^- faces, is less than E_g/e , where e is the elementary charge.

For instance, both DFT and GL theories show that a freestanding BaTiO₃ sample becomes paraelectric below a thickness of 100 Å but remains ferroelectric above this threshold, forming an e^- layer on the P_S^+ surface and a h^+ layer on the P_S^- surface [49–51]. Similar e^- and h^+ layers have

also been suggested to exist at charged domain boundaries [51]. A comparable phenomenon has also been theoretically observed in the hyper-ferroelectric LiBeSb, which remains ferroelectric even at a thickness of 6.08 Å when freestanding in vacuum and features surface e^- and h^+ layers [48].

4. *a*-face Au_2O_3 nanosheets

The above theoretical studies on ferroelectrics [49–51] suggest that placing a freestanding nano-ferroelectric in vacuum can induce a paraelectric phase due to E_d , implying the existence of T_c similar to ferroelectrics. Here, the polar surfaces of Au_2O_3 are *a*-faces.

In light of this, we explore the same possibility in Au_2O_3 , although its unit cell differs substantially from those of conventional displacive-type ferroelectrics. To this end, we examined freestanding *a*-face Au_2O_3 nanosheets with thicknesses of one, two, and five unit cells with a 30-Å-wide vacuum. These values correspond to physical thicknesses of 3.91 Å, 7.81 Å, and 19.4 Å, respectively. Here, $\Delta\phi^{\text{eq,macro}}_{\text{max}}$ represents the built-in potential difference across the vacuum between the top and bottom surfaces.

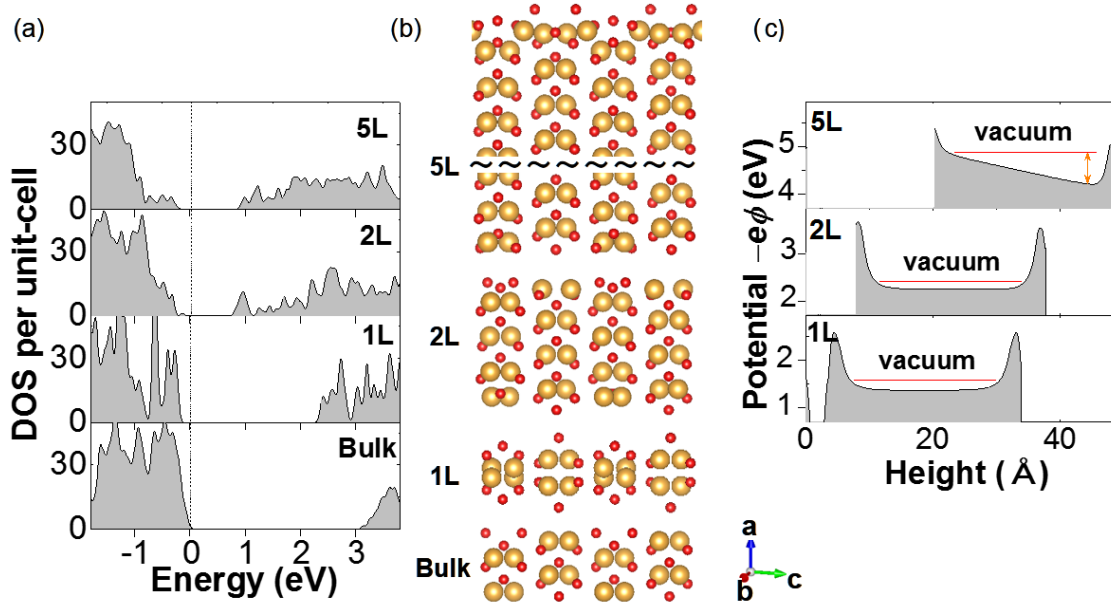


Fig. 6. DOSs of bulk and *a*-face Au_2O_3 nanosheets with thicknesses of 1, 2, and 5 unit cells (L) in vacuum (a), atomic positions (b), and the corresponding potential in vacuum (c). The unit layer of bulk consists of two sub-unit layers that differ only slightly from each other. When P_s is zero and the structure is symmetric along *a*-axis, the potential in vacuum is constant; the horizontal orange lines show a constant potential.

All the examined nanosheets are found to be insulating (Fig. 6(a)). Hence, $\Delta\phi_{\text{macro}}^{eq,\max} = -\int dz E_d(z) = \int dz P(z)/\epsilon_0$, where the integration is from the bottom to top surfaces along a -axis, and P is the total polarization including P_S . For macroscopic systems that ignore surface atomic contributions, $P(z) = P_S$. Because of the periodic boundary condition, this $\Delta\phi_{\text{macro}}^{eq,\max}$ yields $-\Delta\phi_{\text{macro}}^{eq,\max}$ in the vacuum. Hence, $\Delta\phi_{\text{macro}}^{eq,\max} = 0$ means that an average P or a net P_S is zero.

In Fig. 6(b), buckling of the Au–O bonds—that is, the outward displacement of O atoms relative to Au atoms—at the surfaces is evident, consistent with that observed in other oxides [52]. However, the image of the five-unit-cell-thick nanosheet reveals that both Au and O atoms are substantially displaced at the top (P_+) surface, causing the original unit cell to be completely disrupted. In contrast, the relative atomic positions remain nearly unchanged within the inner region, which is located between one unit-cell below the top and half a unit cell above the bottom and has a thickness of 13.4 Å.

Table 5 Inversion symmetry along the a -axis in atom positions of the one-unit-cell-thick Au_2O_3 (having 16 Au and 24 O atoms): comparison of the a -axis coordinates of two Au (a_{Au}) and two O ions (a_{O}) at each c -axis coordinate (c_{Au}) in Å. The centers of mass of a_{Au} ($a_{\text{Au}}^{\text{av}}$) and that of a_{O} (a_{O}^{av}) matched to five decimal places. a_{Au} and a_{O} listed below are obtained by subtracting a_{O}^{av} from the original data.

c_{Au}	0.640	2.606	3.814	5.780	7.059	9.025	10.23	12.199
a_{Au}	0.2828	-0.7596	0.7602	-0.2830	0.2828	-0.7596	0.7602	-0.2830
a_{Au}	-0.2830	0.7602	-0.7596	0.2828	-0.2830	0.7602	-0.7596	0.2828
c_{O}	0	0.925	2.075	3.210	4.344	5.495		
a_{O}	-1.5283	-0.9909	0.5508	1.9972	-0.5503	0.9907		
a_{O}	1.5278	0.9907	-0.5503	-1.9968	0.5508	-0.9909		
c_{O}	6.420	7.344	8.495	9.629	10.764	11.914		
a_{O}	1.5278	-0.9909	0.5508	-1.9968	-0.5503	0.9907		
a_{O}	-1.5283	0.9907	-0.5503	1.9972	0.5508	-0.9909		

In the one-unit-cell-thick nanosheet, Au and O ion positions substantially changed, resulting in inversion symmetry along the a -axis, i.e., the original P_S direction as demonstrated in Fig. 6(b) and Table 5, consistent with the theories mentioned above [48–50]. Accordingly, the nanosheet loses net P_S , as indicated by $\Delta\phi_{\text{macro}}^{eq,\max} = 0$ (Fig. 6(c)) as predicted [48–50]; an inversion symmetric phase can be found by placing a three-dimensional nanoscale ferroelectric in vacuum.

The $\Delta\phi^{eq}_{macro}$ profiles in the one- and five-unit-cell-thick nanosheets in Fig. 5(c) were very similar to those in the nanosheets of prototypical ferroelectrics, which show $P_S = 0$ in thin sheets and $P_S \neq 0$ in thick sheets [49], while Fig. 5(c) displays $\Delta\phi^{eq}_{macro}$ only in vacuum to facilitate the comparisons.

$\Delta\phi^{eq}_{macro}^{max} \neq 0$ in the five-unit-cell-thick nanosheet in Fig. 6(c) indicates the presence of P_S . Furthermore, as mentioned above, the atomic positions in the inner region of the five-unit-cell-thick nanosheet remain nearly identical to those in bulk Au_2O_3 (Fig. 6(b)). This suggests that P_S in the inner region of the nanosheet is similar to that of bulk Au_2O_3 . Therefore, we approximate that the bulk P_S value is preserved in the inner region. In this case, $\Delta\phi^{eq}_{macro}^{max}$ is 320 V ($= 13.4 \text{ \AA} \times P_S / \epsilon_0$) in the absence of any potential screening mechanisms [48]. Similarly, the top surface ($P+$ surface) of a two-unit-cell-thick nanosheet also exhibits evident displacements of O atoms (Fig. 6(b)).

In contrast, the computed $\Delta\phi^{eq}_{macro}^{max}$ is 0.6 V in Fig. 6(c) and less than E_g/e , consistent with theoretical predictions for conventional ferroelectrics [49–51]. Notably, this reduction in $\Delta\phi^{eq}_{macro}^{max}$ for the two- and five-unit-cell-thick Au_2O_3 nanosheets primarily results from surface atomic displacements (reconstructions), unlike in displacive-type ferroelectrics such as PbTiO_3 and BaTiO_3 . Given the thickness dependence of $\Delta\phi^{eq}_{macro}^{max}$ shown in Fig. 6(c) and the occurrence of structural changes only at the surfaces, we conjecture that the built-in potential also exists in thicker sheets and is likely greater than 0.6 eV. The presence of P_S in a freestanding 19.4 \AA -thick-nanosheet and T_C suggests that Au_2O_3 can be classified as hyper-ferroelectric-like.

Conventionally, the screening mechanism of E_d in ferroelectrics without intentional screening materials, such as electrodes, is primarily due to defects and the e^- and h^+ supplied from defects. In ideally prepared ferroelectrics, intrinsic band-excited e^- and h^+ can provide screening [50]. Although often misunderstood, buckling at surfaces [52] is insufficient to screen E_d because it enhances P_S at the $P-$ surface. From this perspective, the substantial screening found in Au_2O_3 reveals a new class of screening mechanism in defect-free insulators.

IV. Conclusion

Because Au oxides form under various application conditions [2–4, 53–59], understanding their properties is essential for advancing related technologies, while bulk forms have been experimentally observed only in Au_2O_3 and Au_2O [10–15]. Among these, merely Au_2O_3 is stable under ambient conditions [16,17], can exist as single crystals [11], and appears in various experiments and applications [53–59]. However, the properties of these oxides, especially Au_2O_3 , have not been much clarified theoretically [25,45]. Hence, this study examined the structural, electronic, dielectric, elastic, and phonon properties of Au_2O_3 and Au_2O , using DFT (PBEsol) and a hybrid functional to ensure accuracy. As benchmark tests, the calculated lattice parameters showed improved agreement with available experimental values compared to previous reports.

These calculations revealed a high degree of functionality in these oxides, including pronounced P_s along the a -axis in Au_2O_3 , which may enhance catalytic activity [31,32]. P_s was retained even in 2-nm-thick nanosheets, yielding a potential of 0.6 V. Because this reduction in potential was caused by the heavy surface reconstruction and the potential increased with thickness (Fig. 6(c)), we conjecture that similar P_s and potentials of comparable magnitudes are present in thicker sheets. Contrastingly, one- and two-unit-cell-thick Au_2O_3 nanosheets lost P_s , and the one-unit-cell-thick nanosheet exhibited inversion symmetry along the a -axis, i.e., the original P_s direction, suggesting a new approach to finding a paraelectric phase. The substantial screening of E_d by heavy surface reconstruction, which has not been reported in typical ferroelectrics, is considered a novel class of screening mechanisms in ideally prepared insulators.

Previous theories have identified Au_2O_3 as a semiconductor with an E_g of 0.85 eV [25,45], which remains a standard to date. The present hybrid functional calculations revealed that Au_2O_3 was an insulator with $E_g = 2.86$ eV. These calculations also indicated that the minimum band gap of stoichiometric Au_2O occurred at the Γ point and was 0.96 eV, 20% greater than the previous theoretical value [25]. The E_g values estimated using PBEsol (GGA) were in agreement with those previously calculated using GGA [24, 25]. The effect of V_O in Au_2O_3 was notably different from that in Ti-oxides, and V_O changed Au_2O_3 into a semiconductor with E_g of 1.3–1.5 eV but retained insulativity.

Finally, Au_2O exhibited unusual softness under shear distortion. Both Au_2O and Au_2O_3

displayed high dielectric constants. DFT and hybrid functional theory calculations revealed no magnetization in stoichiometric Au_2O and Au_2O_3 .

Declaration of Conflicts of Interest The authors declare no competing interests.

Declaration of generative AI use No generative AI was used in this study.

Data availability The data in our manuscript will be obtained from the corresponding author upon request.

Acknowledgments This work was supported partly by the Murata Science and Education Foundation. The discussions with Peter Blöchel of TU Clausthal and Kaushik Dayal of Carnegie Mellon Univ. are greatly acknowledged.

Ref.

1. S.M. Sze and K. Ng Kwok, *Physics of Semiconductor Devices* (John Wiley & Sons, New York 2007). <https://doi.org/10.1002/0470068329>
2. J. Zhang, L. Mou, and X. Jiang, Surface chemistry of gold nanoparticles for health-related applications, *Chem. Sci.* 11, 923 (2020). <https://doi.org/10.1039/C9SC06497D>
3. A. Serva, M. Salanne, M. Havenith, and S. Pezzotti, Size dependence of hydrophobic hydration at electrified gold/water interfaces, *Proc. Natl. Acad. Sci. U.S.A.* 118, e2023867118 (2021). <https://doi.org/10.1073/pnas.2023867118>
4. H. A. Laitinen and M. S. Chao, The anodic surface oxidation of gold, *J. Electrochem. Soc.*, 108, 726 (1961). <https://doi.org/10.1149/1.2428206>
5. J. J. Pireaux, M. Liehr, P. A. Thiry, J. P. Delrue, and R. Caudano, Electron spectroscopic characterization of oxygen adsorption on gold surfaces II. Production of gold oxide in oxygen DC reactive sputtering, *Surf. Sci.* 141, 221 (1984). [https://doi.org/10.1016/0039-6028\(84\)90207-3](https://doi.org/10.1016/0039-6028(84)90207-3)
6. N. Saliba, D. H. Parker, and B. E. Koel, Adsorption of oxygen on Au(111) by exposure to ozone, *Surf. Sci.* 410, 270 (1998). [https://doi.org/10.1016/S0039-6028\(98\)00309-4](https://doi.org/10.1016/S0039-6028(98)00309-4)
7. L. Huang, P. Zeppenfeld, J. Chevrier, G. Comsa, Surface morphology of Au(111) after exposure to oxygen at high temperature and pressure, *Surf. Sci.* 352, 285 (1996). [https://doi.org/10.1016/0039-6028\(95\)01148-X](https://doi.org/10.1016/0039-6028(95)01148-X)
8. M. Haruta, Gold as a novel catalyst in the 21st century: Preparation, working mechanism and applications. *Gold Bull* 37, 27 (2004). <https://doi.org/10.1007/BF03215514>
9. K. Sun, M. Kohyama, S. Tanaka, and S. Takeda, Theoretical study of atomic oxygen on gold surface by Hückel theory and DFT calculations, *J. Phys. Chem. A* 116, 9568 (2012). <https://doi.org/10.1021/jp306906j>
10. E. Schwarzmann and G. Gramann, Darstellung und Eigenschaften von Gold(III)-oxid, *Z. Naturforsch. B* 25B, 1308 (1970).
11. E. Schwarzmann, J. Mohn, and H. Rumpel, Über Einkristalle von Goldoxid Au_2O_3 , *Z. Naturforsch. B* 31B, 135 (1976).

12. P. G. Jones, H. Rumpel, E. Schwarzmann, G. M. Sheldrick and H. Paulus , Gold (III) oxide, *Acta Crystallogr. B* 35, 1435 (1979). <https://doi.org/10.1107/S0567740879006622>
13. N. Weiher, E. A. Willneff, C. Figulla-Kroschel, M. Jansen, and S. L. M. Schroeder. Extended X-ray absorption fine-structure (EXAFS) of a complex oxide structure: a full multiple scattering analysis of the Au L3-edge EXAFS of Au_2O_3 , *Solid State Commun.* 125, 317 (2003).
[https://doi.org/10.1016/S0038-1098\(02\)00817-7](https://doi.org/10.1016/S0038-1098(02)00817-7)
14. M. Higo, M. Mitsushio, T. Yoshidome, S. Nakatake, Characterization of gold oxides prepared by an oxygen-dc glow discharge from gold films using a gold discharge ring by x-ray photoelectron spectroscopy, *Analytical Sciences* 36, 1177, (2020). <https://doi.org/10.2116/analsci.20P065>
15. E. Irissou, M. C. Denis, M. Chaker, and D. Guay, Gold oxide thin film grown by pulsed laser deposition in an O_2 atmosphere, *Thin Solid Films* 472, 49 (2005) <https://doi.org/10.1016/j.tsf.2004.06.092>
16. K. Joshi, A. C. T. Duin, and T. Jacobb, Development of a ReaxFF description of gold oxides and initial application to cold welding of partially oxidized gold surfaces
J. Mater. Chem., 20, 10431 (2010). <https://doi.org/10.1039/c0jm01556c>
17. M. Tang, Y. Zhang, S. Li , X. Wu, Y. Jia, and G. Yang, Mixed-valence compounds: AuO_2 and AuS , *Chem. Phys. Chem.* 19 2989 (2018). <https://doi.org/10.1002/cphc.201800715>
18. A. Filippetti and V. Fiorentini, Coexistence of ionic and metallic bonding in noble-metal oxides, *Phys. Rev. B* 72, 035128 (2005). <https://doi.org/10.1103/PhysRevB.72.035128>
19. J. Zhang, X. Feng, G. Liu, S. A. T. Redfern, and H. Liu,
Computational prediction of a +4 oxidation state in Au via compressed AuO_2 compound, *J. Phys. : Condens. Matter* 32, 015402 (2020). <https://doi.org/10.1088/1361-648X/ab4325>
20. A. Hermann, M. Derzsi, W. Grochala, and R. Hoffmann, AuO : evolving from dis-to comproportionation and back again, *Inorg. Chem.* 55 1278 (2016). <https://doi.org/10.1021/acs.inorgchem.5b02528>
21. L. Schimka, J. Harl, and G. Kresse, Improved hybrid functional for solids: The HSEsol functional, *J. Chem. Phys.* 134, 024116 (2011). <https://doi.org/10.1063/1.3524336>
22. J. Heyd, G.E. Scuseria, M. Ernzerhof, Hybrid functionals based on a screened Coulomb potential, *J. Chem. Phys.* 118, 8207 (2003). <https://doi.org/10.1063/1.1564060>
23. R.-P. Ren, L. Cheng, Y.-K. Lv, Selective oxidation of vinyl chloride on $\text{Ag}_2\text{O}(100)$, $\text{Cu}_2\text{O}(100)$, and $\text{Au}_2\text{O}(100)$ surfaces: A density functional theory study, *Surf. Sci.* 630, 116 (2014).
<http://dx.doi.org/10.1016/j.susc.2014.06.006>
24. F. Pei, S. Wu, G. Wang, M. Xu, S.-Y. Wang, and L.-Y. Chen,
Electronic and Optical Properties of Noble Metal Oxides M_2O ($\text{M} = \text{Cu, Ag and Au}$): First-principles Study, *J. Korean Phys. Soc.* 55, 1243 (2009). <https://doi.org/10.3938/jkps.55.1243>
25. H. Shi, R. Asahi, and C. Stampfl, Properties of the gold oxides Au_2O_3 and Au_2O : First-principles investigation, *Phys. Rev. B* 75, 205125 (2007). <https://doi.org/10.1103/PhysRevB.75.205125>
26. H. Xiao, J. Tahir-Kheli, and W. A. Goddard, III, Accurate Band Gaps for Semiconductors from Density Functional Theory, *J. Phys. Chem. Lett.* 2, 212 (2011). <https://doi.org/10.1021/jz101565j>
27. R. Wahl, D. Vogtenhuber, and G. Kresse, SrTiO_3 and BaTiO_3 revisited using the projector augmented wave method: Performance of hybrid and semilocal functionals *Phys. Rev. B* 78, 104116 (2008).
<https://doi.org/10.1103/PhysRevB.78.104116>

28. D. I. Bilc, R. Orlando, R. Shaltaf, G.-M. Rignanese, J. Íñiguez, and P. Ghosez, Hybrid exchange-correlation functional for accurate prediction of the electronic and structural properties of ferroelectric oxides, *Phys. Rev. B* 77, 165107 (2008). <https://doi.org/10.1103/PhysRevB.77.165107>

29. Y. Watanabe, Calculation of strained BaTiO₃ with different exchange correlation functionals examined with criterion by Ginzburg-Landau theory, uncovering expressions by crystallographic parameters, *J. Chem. Phys.* 148, 194702 (2018). <https://doi.org/10.1063/1.5022319>

30. Y. Watanabe, DFT + *U* accurate for strain effect and overall properties of perovskite oxide ferroelectrics and polaron, *J. Appl. Phys.* 135, 224103 (2024). <https://doi.org/10.1063/5.0213487>

31. C. Zhen, Z. Ren, Y. Kang, L. Wang, and G. Liu, PbTiO₃-based single-domain ferroelectric photocatalysts for water splitting, *Acc. Mater. Res.* 4, 591 (2023). <https://doi.org/10.1021/accountsmr.3c00042>

32. J. He, Y. Liu, J. Qu, H. Xie, R. Lu, F. Fan, and C. Li, Boosting photocatalytic water oxidation on photocatalysts with ferroelectric single domains, *Adv. Mater.* 35, 2210374 (2023).
<https://doi.org/10.1002/adma.202210374>

33. C. Biz, J. Gracia and M. Fianchini, Review on magnetism in catalysis: from theory to PEMFC applications of 3d metal pt-based alloys, *Int. J. Mol. Sci.* 2022, 23, 14768. <https://doi.org/10.3390/ijms232314768>

34. P. E. Blöchl, Projector augmented-wave method. *Phys. Rev. B* 50, 17953 (1994). <https://doi.org/10.1103/PhysRevB.50.17953>

35. G. Kresse and J. Hafner, Ab initio molecular dynamics for liquid metals. *Phys. Rev. B* 47, 558R (1993). <https://doi.org/10.1103/PhysRevB.47.558>

36. G. Kresse and J. Furthmüller, Efficiency of *ab-initio* total energy calculations for metals and semiconductors using a plane-wave basis set. *Comput. Mater. Sci.* 6, 15 (1996). [https://doi.org/10.1016/0927-0256\(96\)00008-0](https://doi.org/10.1016/0927-0256(96)00008-0)

37. G. Kresse and D. Joubert, From ultrasoft pseudopotentials to the projector augmented-wave method. *Phys. Rev. B* 59, 1758 (1999). <https://doi.org/10.1103/PhysRevB.59.1758>

38. J. P. Perdew, A. Ruzsinszky, G. I. Csonka, O. A. Vydrov, G. E. Scuseria, L. A. Constantin, X. Zhou, and K. Burke, Restoring the density-gradient expansion for exchange in solids and surfaces. *Phys. Rev. Lett.* 100, 136406 (2008). <https://doi.org/10.1103/PhysRevLett.100.136406>

39. H. J. Monkhorst and J. D. Pack, Special points for Brillouin-zone integrations, *Phys. Rev. B* 13, 5188 (1976). <https://doi.org/10.1103/PhysRevB.13.5188>

40. R. Resta, Theory of the electric polarization in crystals, *Ferroelectr.* 136, 51 (1992). <https://doi.org/10.1080/00150199208016065>

41. Y. Watanabe, Ferroelectricity of stress-free and strained pure SrTiO₃ revealed by *ab initio* calculations with hybrid and density functionals, *Phys. Rev. B* 99, 064107 (2019). <https://doi.org/10.1103/PhysRevB.99.064107>

42. M. Hacene, A. A. Sedrakian, X. Rozanska, D. Klahr, T. Guignon, and P. F. Lessard, Accelerating VASP electronic structure calculations using graphic processing units. *J. Comput. Chem.* 33, 2581 (2012). <https://doi.org/10.1002/jcc.23096>

43. M. Hutchinson and M. Widom, VASP on a GPU: Application to exact-exchange calculations of the stability of elemental boron. *Comput. Phys. Commun.* 7, 1422 (2011). <https://doi.org/10.1016/j.cpc.2012.02.017>

44. K. Momma and F. Izumi, VESTA 3 for three-dimensional visualization of crystal, volumetric and morphology data. *J. Appl. Crystallogr.* 44, 1272 (2011). <https://doi.org/10.1107/S0021889811038970>

45. Materials Project <https://next-gen.materialsproject.org/materials/mp-27253>

46. M. Hakimzadeh, C. Mora-Corral, N. Walkington, G. Buscarnera, and K. Dayal, Phase-field modeling of fracture under compression and confinement in anisotropic geomaterials, *Int. J. Numer. Anal. Methods Geomech.* 49, 1319 (2025). <https://doi.org/10.1002/nag.3933>

47. V. Wang, N. Xu, J.-C. Liu, G. Tang, W.-T. Geng, Vaspkit: A|user-friendly interface facilitating high-throughput computing| and analysis using VASP code, *Comput. Phys. Commun.* 267, 108033, (2021). <https://doi.org/10.1016/j.cpc.2021.108033>

48. Y. Watanabe, Breakdown of ion-polarization-correspondence and born effective charges: Algebraic formulas of accurate polarization under field, *Phys. Rev. Materials* 4, 104405 (2020). <https://doi.org/10.1103/PhysRevMaterials.4.104405>

49. Y. Watanabe, Examination of permittivity for depolarization field of ferroelectric by ab initio calculation, suggesting hidden mechanisms, *Sci. Rep.* (2021) 11:2155 | <https://doi.org/10.1038/s41598-021-81237-0>

50. Y. Watanabe, Theoretical stability of the polarization in a thin semiconducting ferroelectric, *Phys. Rev. B* 57, 789 (1998). <https://doi.org/10.1103/PhysRevB.57.789>

51. Y. Watanabe, M. Okano, and A. Masuda, Surface conduction on insulating BaTiO₃ crystal suggesting an intrinsic surface electron layer, *Phys. Rev. Lett.* 86, 332 (2001). <https://doi.org/10.1103/PhysRevLett.86.332>

52. R.I. Eglitis and R. Jia, Review of systematic tendencies in (001), (011) and (111) surfaces using B3PW as well as B3LYP computations of BaTiO₃, CaTiO₃, PbTiO₃, SrTiO₃, BaZrO₃, CaZrO₃, PbZrO₃ and SrZrO₃ perovskites, *Materials* 16, 7623 (2023). <https://doi.org/10.3390/ma16247623>

53. D. Degerman, S. B. Bibi, B. Davies, V. Grigorev, A. Kalinko, T. Hansson, and S. Koroidov, X-Ray Absorption Spectroscopy Probing of Gold Electro-Oxidation Reveals Intermediate Surficial Au(I), *ChemElectroChem* 12, e202500127 (2025) <https://doi.org/10.1002/celc.202500127>

54. Y. Yamamoto, S. Arai, A. Esaki, J. Ohyama, A. Satsuma, and N. Tanaka, Statistical distribution of single atoms and clusters of supported Au catalyst analyzed by global high-resolution HAADF-STEM observation with morphological image-processing operation, *Microscopy* 63, 209, (2014), <https://doi.org/10.1093/jmicro/dfu001>

55. Y. Momose, Triboelectrification of Metals brought into Sliding Contact with Polytetrafluoroethylene: Influence of Metal Oxide Formation Energy, P. K. Bhowmik ed., Chemical and Materials Sciences - Developments and Innovations 2, 144 (2024, B P International). <https://doi.org/10.9734/bpi/cmsdi/v2>

56. Y. Chen, C. W. Li, and M. W. Kanan, Aqueous CO₂ Reduction at Very Low Overpotential on Oxide-Derived Au Nanoparticles, *J. Am. Chem. Soc.* 134, 19969 (2012). <https://doi.org/10.1021/ja309317u>

57. L. Shan, Physical and Chemical Properties of Size-selected Supported Nanostructures, Thesis, KU Leuven <http://hdl.handle.net/1942/20149>

58. W. C. Coral, Microstructure, chemistry and optical properties in ZnO and ZnO-Au nanocomposite thin films grown by DC-reactive magnetron co-sputtering, Thesis, Université de Lorraine, <http://dx.doi.org/10.22028/D291-23065>

59. K. Kennedy, Md R. Adib, K. Rönnby, I. Seymour, M. Nolan, M. Fenelon, A. O'Riordan, Gold/Gold Oxide as a Solid State On-Chip pH Sensing Probe, *ChemRxiv* 23 September 2025 <https://doi.org/10.26434/chemrxiv-2025-rzr9m>